JOURNAL OF SPACECRAFT AND ROCKETS
Vol. 44, No. 3, May–June 2007

Heat Flux Measurements for a GO_2/GH_2 Single-Element, Shear Injector

Alex Conley,* Aravind Vaidyanathan,† and Corin Segal‡
University of Florida, Gainesville, Florida 32611

DOI: 10.2514/1.26678

A new, high-pressure facility was used to investigate GO_2/GH_2 single-element, shear, coaxial injectors with operating conditions typical of rocket engines. Oxygen-to-hydrogen mass flow ratios of 4 and 6 at operational chamber pressures of 6.2, 4.9, 4.5, and 2.8 MPa were investigated by 1) keeping the propellant mass flow rates constant while changing the exhaust nozzle diameter, and 2) by keeping the exhaust nozzle diameter constant and changing the propellant mass flow rates to change the chamber pressure. Axial heat fluxes, injector face temperature, and exit nozzle temperature were measured. The injector's outer diameter was 2.7 mm and the chamber cross section was square with a side $L = 2.5$ cm. Maximum heat release occurred at 2.4 L from the injector face. The injector face temperatures showed little to no dependence on chamber pressure except for high mass flow ratios. A clear dependence exists, however, on the chamber length. The profiles of heat flux and chamber wall temperatures indicated no pressure dependence and only a slight dependence on propellant injection velocities when the mass flows were kept constant. A scaling of heat flux values based on fuel mass flow rate, instead of chamber pressure, is, therefore, suggested. The lack of pressure dependence and only slight dependence on the propellant injection velocities suggested that the basic dynamic structures of the combusting flow were mainly dominated by the chamber geometry.

Nomenclature

A	=	area, m^2
C_p	=	heat capacity, $J/(kg \cdot K)$
C_v	=	valve flow coefficient
d_j	=	oxygen OD jet diameter, mm
k	=	thermal conductivity, $W/(m \cdot K)$
M	=	Mach number
$\dot{m}$	=	mass flow rate, g/s
O/F	=	oxygen-to-fuel ratio
p	=	pressure, MPa
Q	=	volumetric flow rate
q_A	=	heat flux per unit area, W/m^2
R	=	gas constant, $m^2/s^2/T$
SG	=	specific gravity
T	=	temperature, K
T_{wall}	=	chamber wall temperature, K
t	=	time, s
u	=	velocity, m/s
x	=	axial distance, m
γ	=	specific heat ratio
ρ	=	density, kg/m^3
Φ	=	equivalence ratio, $(m_{O2}/m_{H2})_{\text{actual}}/(m_{O2}/m_{H2})_{\text{stoichiometric}}$

Subscripts

o	=	oxygen
h	=	hydrogen
0	=	stagnation conditions

Received 20 July 2006; revision received 1 December 2006; accepted for publication 7 December 2006.

*Graduate Research Assistant, currently at CFDRC, Huntsville, Al.
†Graduate Research Assistant, Mechanical and Aerospace Department.
‡Associate Professor, Mechanical and Aerospace Department. Associate Fellow AIAA.

I. Introduction

CONSIDERABLE efforts exist to model combustion in rocket chambers and calculate the conjugate heat transfer to the walls [1]. These efforts have met only partial success so far and require comprehensive experimental data, including wall heat fluxes and inflow measurements, that is, species concentration, velocity distribution, etc., for validation. To date, sets of data have been generated in various facilities covering different ranges of pressure, mass flows, and, in certain cases, inflow data. There is, still, a need to acquire a comprehensive set of data in the same facility over a broad range of conditions to facilitate the development and validation of computational models before computational fluid dynamics (CFD) becomes an effective design tool for rocket combustion chambers, components' performance, or cooling systems [2]. Most CFD model results in the past have been based on steady-state 2-D analyses of the largely unsteady and 3-D processes in the rocket combustion chamber; only recently has investigation into unsteady combustion systems begun. Furthermore, heat transfer into the combustor walls has rarely been addressed, even though the strength, life cycle, and cooling system effectiveness are highly dependent on the heat transfer into and out of the chamber wall [3]. Although several experimental studies of high-pressure combustion systems have been conducted [4–9], the facilities were of different sizes, internal geometries, fuel composition, and injection configuration and, therefore, the heat release and wall heat fluxes were different, as were the chamber dynamics. All facilities listed above included optical access to measure inflow parameters. Additional studies of wall heat fluxes were done in a windowless chamber with detailed wall instrumentation [10]. These studies covered different operational regimes, targeted a host of combustion applications—for example, gas-turbine combustors [4]—and different fuel systems from gaseous oxygen/hydrogen [8] to liquid hydrocarbons [7]; most were disconnected from a parallel computational effort.

The experimental facility used in this study was designed to optimize the, sometimes contradictory, requirements of experimental testing and CFD modeling and provide heat fluxes, inflow data, and accurate boundary conditions up to 60 atm for a single-element, shear injector to generate a broad range of data for code validation. In the study presented here wall heat fluxes were measured for a GH_2/GO_2 system with mass flow ratios, $\dot{m}_{O_2}/\dot{m}_{H_2} = 4$ and 6 and chamber pressures in the range of 20–60 atm. The chamber pressure was adjusted by 1) changing the mass flows, thus

Table 1 Coaxial-shear injector features comparison. Includes UF, Penn State, SSME, and GGIT injectors

	UF 1	UF 2	PSU	SSME	GGIT 1	GGIT 2	GGIT 3	GGIT 4
ID of O_2 post, in. (mm)	0.0472 (1.2)	0.0591 (1.5)	0.3051 (7.75)	0.0876 (2.226)	0.173 (4.394)	0.173 (4.394)	0.173 (4.394)	0.173 (4.394)
ID of H_2 annulus, in. (mm)	0.0866 (2.2)	0.0984 (2.5)	0.3752 (9.53)	0.148 (3.76)	0.203 (5.156)	0.203 (5.156)	0.203 (5.156)	0.203 (5.156)
OD of H_2 annulus, in. (mm)	0.1058 (2.687)	0.1058 (2.687)	0.5 (12.7)	0.1980 (5.03)	0.227 (5.766)	0.231 (5.867)	0.235 (5.969)	0.249 (6.325)
O_2/H_2 injection area ratio	0.6	2.32	0.85	——	2.9	2.46	2.14	1.44
O_2/H_2 velocity ratio	0.1–0.7	0.1–0.5	0.29	——	0.126	0.148	0.17	0.257
O_2/H_2 mass flow ratio	1.0–6.0	3.7–18.2	4.0	——	5.9	5.9	5.9	5.9
Φ	8.25–1.33	2.15–0.44	1.98	——	1.35	1.35	1.35	1.35
Chamber pressure, atm	0–60	0–60	12.9	——	75	75	75	75

keeping the injection velocities constant and 2) by maintaining the mass flows constant and changing the chamber exit area. In this case the injection velocities changed accordingly; however, the velocity and density ratios remained constant. Wall heat fluxes, injector face temperatures, and exit nozzle temperatures were measured. In addition, instantaneous broadband flame emission images and average broadband flame emission images were obtained for selected conditions. These images are useful to indicate flame liftoff distance, shear layer growth, instantaneous flame propagation phenomena, and average flame speeds.

II. Experimental Facility

The high-pressure combustion experimental facility used in this study was designed to allow optical access for flow diagnostics. The injectors are coaxial, shear, single element designed to match geometrical parameters of injectors used in previous work [8,11]. Table 1 lists the main geometrical and operational parameters of the two injectors used at the University of Florida—UF 1 and UF 2—which are shown schematically in Fig. 1. Included in the table are the Pennsylvania State University (Penn State) facility used for optical diagnostics [9] and the four injectors' geometries used during the gas-gas injector technology (GGIT) program [11]. The space shuttle main engine (SSME) injectors' dimensions are also included to indicate the relative proportionally of these different designs. The UF injectors are close to half the dimension of the SSME injectors and close to 5 times smaller than the Penn State injectors. The GGIT injectors have an oxidant inside diameter (ID) and outside diameter (OD) close to twice the size of the SSME injectors and differ among each other by the hydrogen OD thereby maintaining the oxidant post thickness the same. The post oxidant post thickness plays a significant role in flameholding and the development of the shear layers and was also maintained constant in the UF injectors' configuration at 0.5 mm. This is close to the GGIT post thickness, which was 0.42 mm in all configurations and close to half the size of the Penn State oxidizer post of 0.9 mm. The SSME post thickness is 0.75 mm. The O/F velocity ratio in the UF facility ranges between 0.1–0.7 covering the range of conditions of the other injectors in the table. The mass flow ratios cover a broad range, in particular, when the UF 2 injector is considered, considerably larger than normally practiced in practical applications to expand the capability to provide a broad range of results for comprehensive code validation. Finally, the facility operates with pressures up to 60 atm which is close to the range used in the GGIT studies and a second high-pressure facility used at Penn State [10], which is axisymmetric rather than 2-D as the UF facility.

Figure 2 shows a schematic of the UF facility indicating the modular construction. The chamber is made of copper given the high

	UF1	UF2
D1, in(mm)	0.047 (1.2)	0.059 (1.5)
D2, in(mm)	0.087 (2.2)	0.098 (2.5)
D3, in(mm)	0.106 (2.7)	0.106 (2.7)

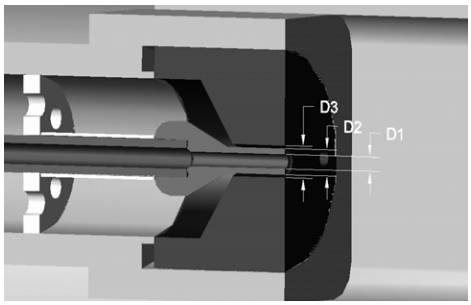

Fig. 1 Injectors detail.

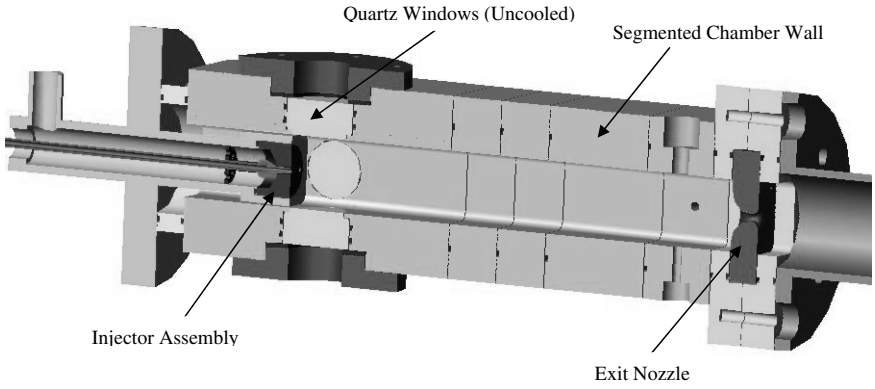

Fig. 2 Combustion chamber configuration. The injector location can be adjusted to access optically different regions of the flame. The chamber length can be modified by positions of the chamber section resulting in over 25 chamber lengths.

thermal conductivity of the material. The chamber's cross section is 2.5×2.5 cm^2 (1 in. square) with large, 3 mm, corner radius to reduce stress concentration areas and hot spots while allowing maximum optical access capabilities. The modular construction allows chamber length modification over 25 different configurations to evaluate the chamber length effect on the flowfield recirculation regions and to permit the placement of the windows at different locations. The windows are made of UV-grade fused silica with a softening temperature above 1600°C and transmissivity as low as 225 nm. The windows are 2.5 cm in diameter and are 1.25 cm thick. They are placed on four sides of the chamber allowing a viewable field of 19 mm diameter. The windows are uncooled and the inner sides include a machined step to guarantee that the windows were flush with the internal chamber wall.

To further facilitate geometrical changes the injector design provides the ability for recessed, flush, and protruding oxidizer post configurations. A spacer sleeve and a spacer baffle are used to hold the oxidizer nozzle in the center of the injector housing. The spacer baffle supports the oxidizer tube and further serves to uniformly distribute the fuel flow around the oxidizer nozzle.

Other facility components include the exhaust nozzle which incorporates temperature measurement for accurate prediction of boundary conditions in computations, the ignition source, and the gases supply system.

A diagram of the gases supply and purge system is shown in Fig. 3. The propellant feed system can provide either gaseous oxygen (GO_2) or air as the oxidizer and gaseous hydrogen (GH_2) as the fuel. The entire system is a pressure fed system, meaning there are no pumps and the propellants and the nitrogen are all supplied via high-pressure gas bottles. The GO_2 supply is provided by an array of 10 bottles at 17.9 MPa (2600 psi) connected in parallel and the GH_2 supply is provided by a single hydrogen bottle at 17.9 MPa (2600 psi). This combination provides sufficient fuel for 20–30 tests depending on the test lengths, which are normally limited to 6 s from ignition. The purge is provided by pressurized nitrogen connected to the fuel and oxidizer lines such that it purges the lines from the supply systems downstream. This nitrogen system also offers the capability to prepressurize the chamber immediately before the combustion test. The gases mass flows are controlled through choked needle valves with the flow rate coefficient determined precisely from the metering valve micrometric vernier. Solenoid valves open and close the gas lines in a sequence controlled by the control and data acquisition system. A detailed description of the facility, the data acquisition, and control is given in [12].

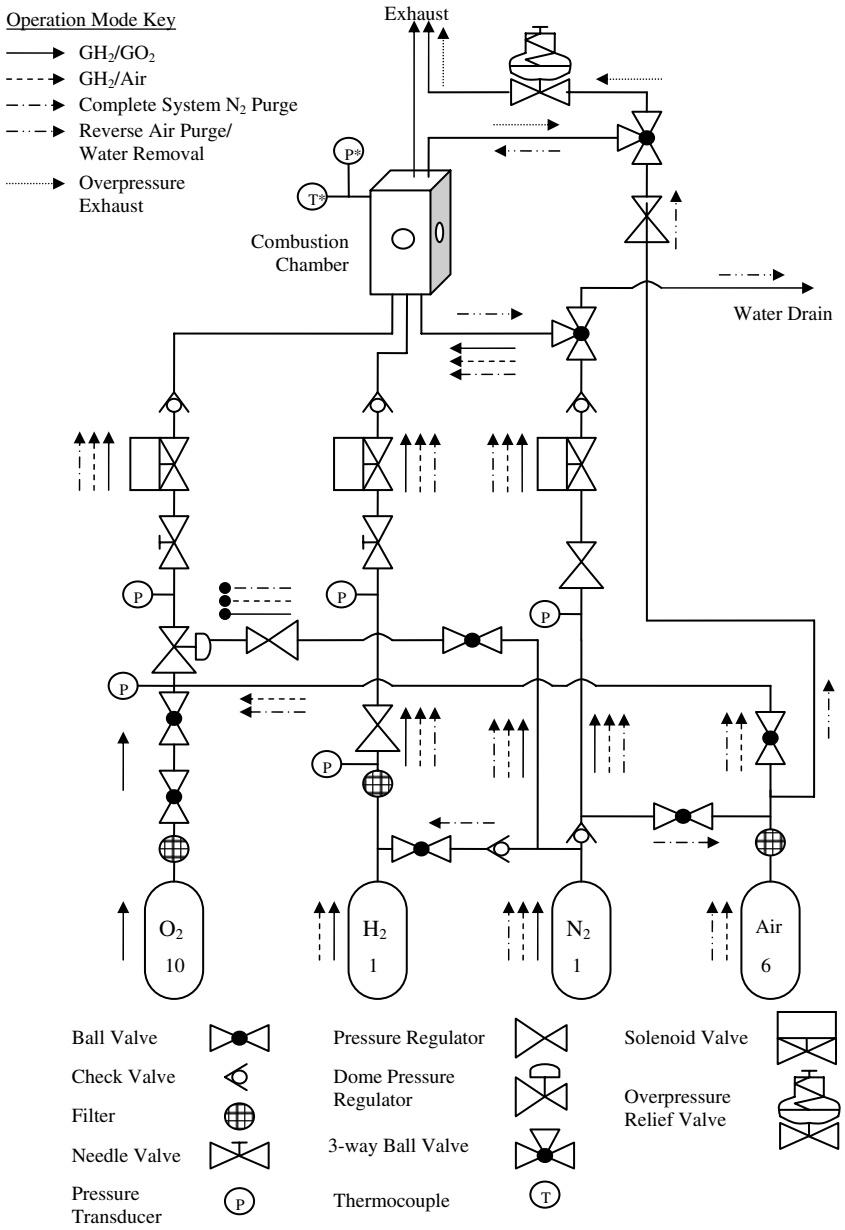

Fig. 3 Schematic diagram of the facility propellant/purge feed system.

Table 2 Experimental conditions: group A: $m_{O2}/m_{H2} = 4$, $m_{H2} = 0.396$ g/s, ID_{nozzle} variable, $L_{chamber}$ fixed. Group B: $m_{O2}/m_{H2} = 6$, $m_{H2} = 0.285$ g/s, ID_{nozzle} variable, $L_{chamber}$ fixed. Group C: $m_{O2}/m_{H2} = 4$, $m_{H2} = 0.396$ g/s, ID_{nozzle} fixed, $L_{chamber}$ variable. Group D: $m_{O2}/m_{H2} = 4$, m_{H2} = variable, ID_{nozzle} fixed, $L_{chamber}$ fixed

	P, MPa	O/F, mass flow	O/F, velocity	Φ	Hydrogen mass flow, g/s	Hydrogen velocity, m/s	Exit nozzle ID, mm	Chamber length, mm
Group A	6.21	4	0.41	2.0	0.396	42.52	1.36	169.3
	4.86	4	0.41	2.0	0.396	54.33	1.59	169.3
	4.55	4	0.41	2.0	0.396	58.03	1.70	169.3
	2.76	4	0.41	2.0	0.396	95.67	2.38	169.3
Group B	6.21	6	0.62	1.33	0.285	30.60	1.36	169.3
	4.86	6	0.62	1.33	0.285	39.10	1.59	169.3
	4.55	6	0.62	1.33	0.285	41.76	1.70	169.3
	2.76	6	0.62	1.33	0.285	74.53	2.38	169.3
Group C	4.86	4	0.41	2.0	0.396	54.33	1.59	150.7
	4.86	4	0.41	2.0	0.396	54.33	1.59	132.1
	4.86	4	0.41	2.0	0.396	54.33	1.59	112.6
	4.86	4	0.41	2.0	0.396	54.33	1.59	94.0
Group D	2.75	4	0.41	2.0	0.187	45.34	1.70	169.3
	3.90	4	0.41	2.0	0.280	47.87	1.70	169.3
	4.93	4	0.41	2.0	0.377	50.99	1.70	169.3
	5.87	4	0.41	2.0	0.470	53.39	1.70	169.3

A. Heat Flux Calculation

The chamber extensions shown in Fig. 2 incorporate heat flux sensors made of thermocouple pairs placed next to each other and separated by 7 mm in a transverse direction. The temperature gradient measured at each axial location is used to infer the local heat flux. Because the walls do not achieve thermal steady conditions during the 5–6 s experiment the Fourier law for heat transfer must be corrected with an unsteady term that accounts for the heat accumulated in the walls, as follows:

$$q_A = \frac{k}{\Delta x}(T_{i,2} - T_{o,2}) + \frac{\rho c \Delta x}{2}\frac{(T_{o,2} - T_{o,1})}{\Delta t} \tag{1}$$

Here, the density γ and heat capacity c for copper 110 are 8700 kg/m^3 and 385 J/(kg · K), respectively. The temperature subscript i represents the thermocouple closest to the inner chamber wall, o represents the thermocouple farthest from the inner chamber wall, "1" represents an initial time, and "2" represents a final time. In Eq. (1), q_A is the heat flux per unit area obtained from the experiment using Δx as the distance between any thermocouple pair. The nonsteady component mounted to 5–10% of the total heat flux.

III. Results

A. Wall Heat Fluxes

The experiments described below used a GH_2/GO_2 system with O/F mass flow ratios of 4 and 6 ($\Phi = 2.0$ and 1.33) and chamber pressure ranging from 2.8 to 6.2 MPa. Table 2 includes a list of the experiments grouped in four sets. The first two sets, groups A and B, included experiments with mass flow ratios of 4 and 6, respectively, during which the gases mass flows were kept constant and the chamber pressure was adjusted by changing the exit nozzle orifice. The third set, group C, evaluated the effect of chamber length while maintaining all other parameters constant. Finally, the fourth set, group D, maintained a fixed geometry and mass flow ratio at 4, achieving chamber pressure changes by changing the gases mass flows. Complete sets of data are listed in [12]. The resulting gas injection and chamber flows were turbulent.

Figures 4 and 5 show the pressure rise and wall heat fluxes, respectively, for an experiment with chamber pressure of 4.86 MPa and $O/F = 4$ indicating that full steady conditions were not recorded during the 8 s test. The figures indicate that at certain locations the heat fluxes have reached steady state while the pressure tends to rise slightly caused by the thermal expansion of the uncooled exit nozzle. In all of the following figures the heat fluxes were calculated toward the end of the experiment when steady state is essentially reached at all axial locations. Instantaneous, 500 ns images of the flame shown in Fig. 6 indicate the onset of jet instabilities at $4d_j$. These images are direct photography and, therefore, integrate through the jet. They are due, mostly, to water emission in the visible range [13] with additional chemilluminesence from OH. An average of 132 instantaneous images shown in Fig. 7 indicates the formation of the "dark" core, a parameter that is used at times to verify computational prediction, with a length of $6d_j$. The flame liftoff distance can be estimated from this image and is found as 1 mm at these experimental conditions. Additionally, the shear layer is seen to bend toward the centerline, that is, toward the oxidizer as it develops away from the injector, which is characteristic of fuel-rich shear layers [14].

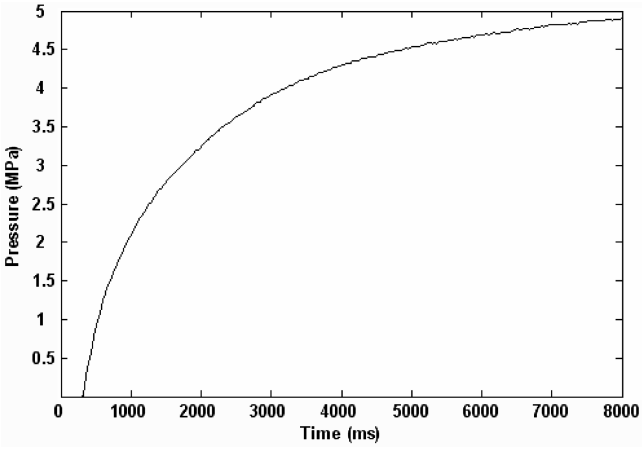

Fig. 4 Chamber pressure versus time for $P_{chamber} = 4.86$ MPa, $m_{O2}/m_{H2} = 4$ and $v_{O2}/v_{H2} = 0.46$. The plot indicates that pressure steady state is not fully achieved during the 8 s sequence.

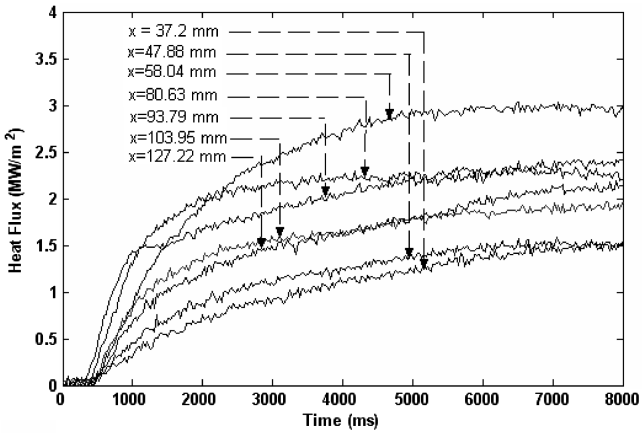

Fig. 5 Heat flux for $P_{chamber} = 4.86$ MPa, $m_{O2}/m_{H2} = 4$. The legend indicates the heat fluxes axial distance from the injector face.

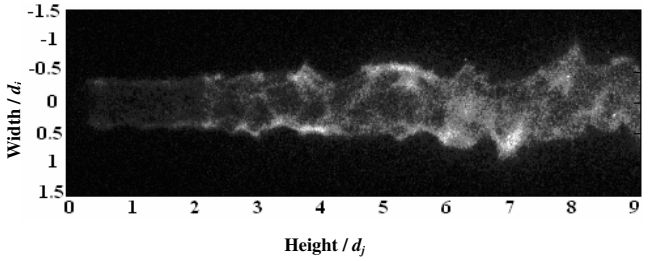

Fig. 6 Instantaneous flame image at $P_{\text{chamber}} = 4.86$ MPa, $O/F = 4$, $m_{\text{H2}} = 0.396$ g/s, and $v_{\text{O2}}/v_{\text{H2}} = 0.46$. Broadband flame emission with exposure time of 500 ns indicates the jet instabilities forming at 4 jet diameters.

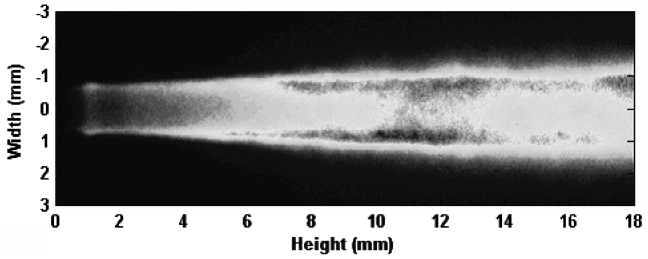

Fig. 7 An average of 132 instantaneous images. Most of the emission is due to OH and water hence the averaged image indicates the length of the dark core. At these experimental conditions the dark core is 6 jet diameters.

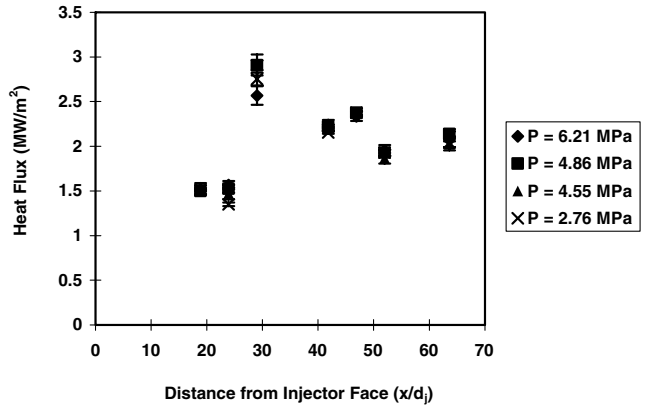

Fig. 8 Wall heat fluxes for $O/F = 4.0$ and constant mass flow rates. The exit nozzle area was changed to modify chamber pressure. The heat flux profiles are independent of pressure.

Figures 8 and 9 show the wall heat fluxes determined for $O/F =$ 4.0 and 6.0, respectively, with constant mass flows and variable exit area to change the chamber pressure. The heat fluxes are independent of pressure in these cases because the mass flow remains constant and the change in heat transfer caused by velocity changes through the Reynolds number is negligible. The differences over more than twofold pressure increase remained below 18% at the location sensitive to displacement of the stagnation point and below 8% at all other locations. This includes the accuracy of the heat flux measurement evaluated as 2%.

The heat fluxes show a maximum of 3.2 and 3.4 MW/m^2, respectively, at $30d_j$ from the injector face, further decaying slowly in the axial direction toward the chamber exit. The chamber wall temperature plot, determined analytically from the heat fluxes, indicates that the wall temperatures increase, peak, and decrease along the length of the chamber, as shown in Fig. 10. This seems to indicate that the shear layer, the hottest portion of the flame, contacts the chamber wall at the location of the peak wall temperature, or around 83 mm, that is, $41d_j$, from the injector face. This location is the same for both equivalence ratios. However, the distance from the injector face at which the highest heat release occurs appears to be around $30d_j$ from the injector face. The maximum heat release location appears to have little dependence on mass flow ratio and

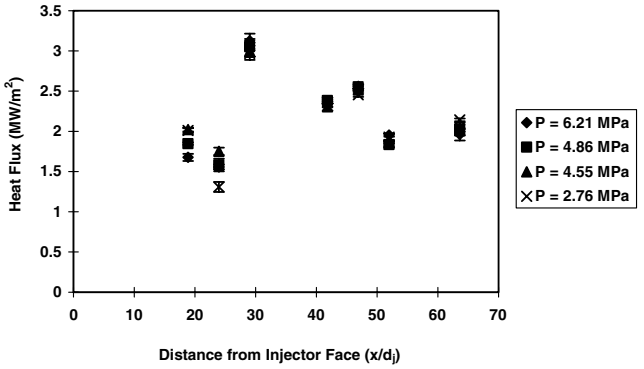

Fig. 9 Wall heat fluxes for $O/F = 6.0$ and constant mass flow rates.

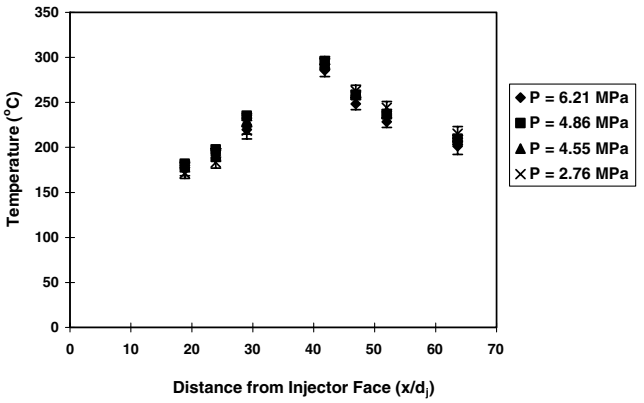

Fig. 10 Wall heat temperatures inferred from heat fluxes at $O/F = 4$.

injection velocities, and no pressure dependence. Because the heat fluxes and chamber wall temperature profiles did not seem to be affected by changes in chamber pressure, mass flow ratios, velocity ratios, and injection velocities, they would appear to be dominated mainly by geometrical features.

When the exit nozzle area is fixed and the gases mass flows are changed thereby changing the chamber pressure the heat fluxes change with the mass flow and the resulting chamber pressure change as shown in Fig. 11. Scaling all heat flux data with chamber pressure raised at a power of 0.6 normalizes the entire data set, as shown in Fig. 12a, similar to the findings in [10]. The fact that the profile remains similar across all pressures suggests that the dynamic structures within the combusting flow are pressure independent if all other factors remain constant. Furthermore, the results from the combustion tests where the mass flow rates were held constant, in which the injection velocities must increase for the same injector geometry, indicate that the dynamic structures within the combusting flow are only slightly dependent on the injection velocity, as indicated by slightly varying values in the heat fluxes with similar profiles. This suggests that the basic dynamic structures of the combusting flow are mostly dependent on the chamber geometry, with little dependence on injection velocities and no pressure dependence.

The scaling with chamber pressure is useful in cases when the chamber nozzle is kept constant. It fails, however, for experiments when the mass flow is kept constant and the chamber pressure is varied by changing the exhaust nozzle diameter. In these cases a scaling based on the square root of the mass flow normalizes all the data as indicated in Fig. 12b. This scaling is a preferable choice because it satisfies all conditions irrespective of the chamber geometry and it satisfies both sets of data with and without constant exit area. Clearly, the wall heat fluxes will scale with the Reynolds number, given that the other major parameter in any Nusselt number formulation, the Prandtl number next to the wall remains relatively unchanged. That correlation, however, is more complex and subject to a more detailed convective heat flux analysis; for a first approximation, the square root of the mass flow appears to be a reasonably accurate parameter.

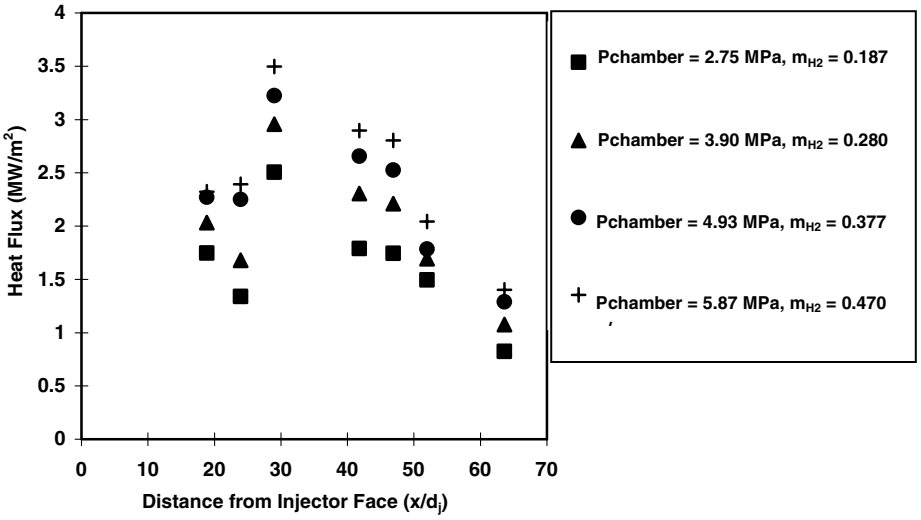

Fig. 11 Wall heat fluxes for $O/F = 4.0$ with variable mass flows and constant exit nozzle.

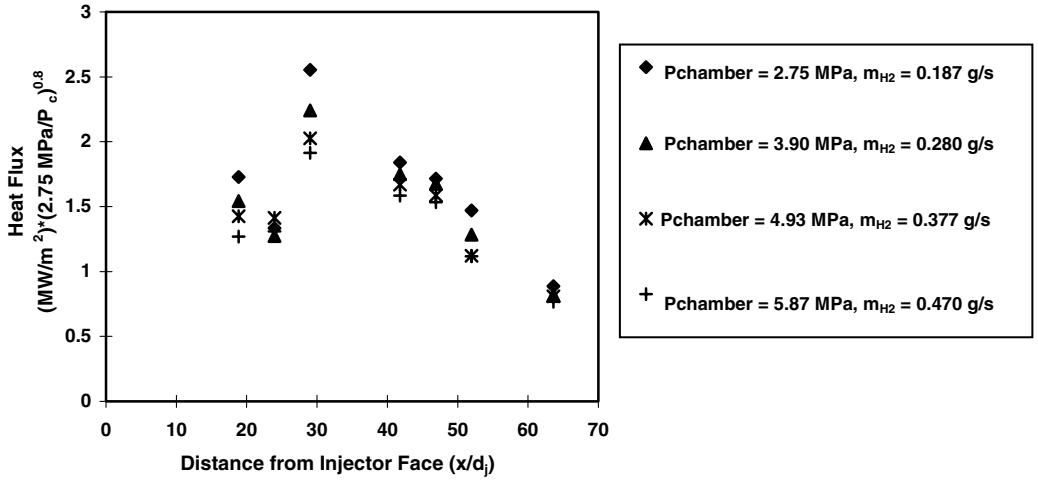

a) Heat flux values scaled with chamber pressure

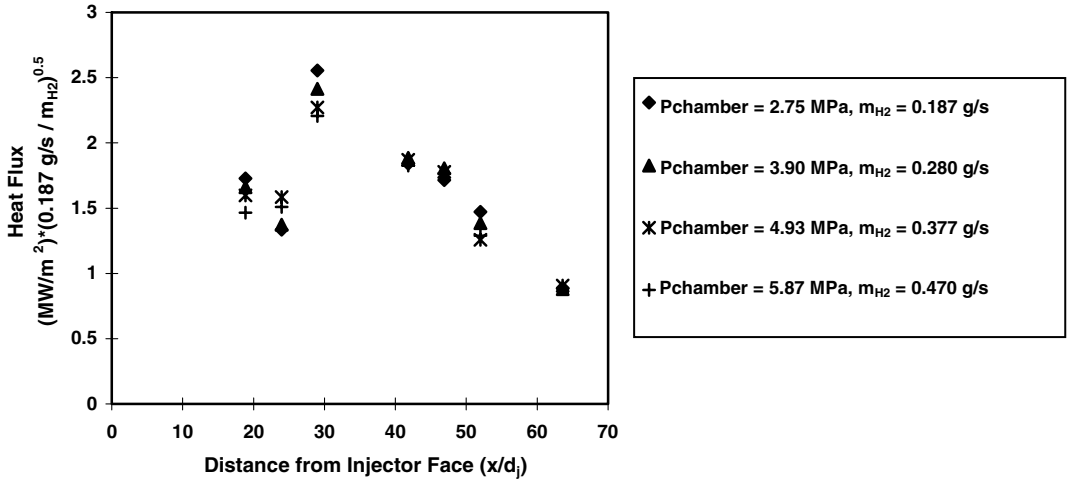

b) Heat flux values scaled with mass flow

Fig. 12 a) Heat flux values scaled with the chamber pressure for $O/F = 4.0$; b) square root scaling with mass flow normalized wall heat fluxes irrespective of the experimental method used to change the chamber pressure for $O/F = 4.0$.

B. Injector Face Temperature

The injector face temperatures for O/F mass flow of 4 show little pressure dependence, as shown in Fig. 13. Two locations were measured at 2.1 and 4.2 mm from the injector center axis. The bars on the data points indicate the range of fluctuation recorded during the experiment at each location indicating, in all cases, that larger temperature fluctuations are recorded at the location closer to the injector. There is a noticeable increase in face temperature as pressure increases at the larger $O/F = 6$ as noticed in Fig. 14. Moreover, at the higher mass flow ratio, the injector face

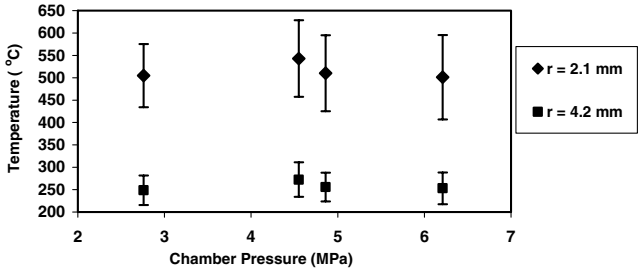

Fig. 13 Injector face temperatures at $O/F = 4.0$. Temperatures are measured at 2.1 and 4.2 mm from the injector center. Bars indicate the temperature fluctuation. There appears to be no dependence on chamber pressure at this mass flow ratio.

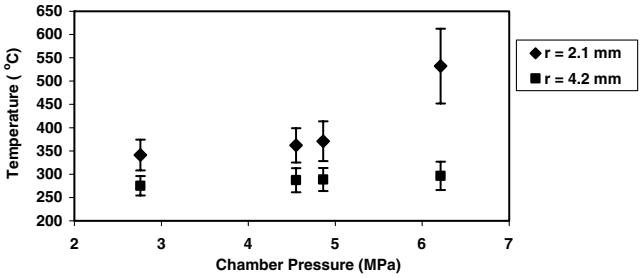

Fig. 14 Injector face temperatures at $O/F = 6$. An increase in temperature is recorded as the chamber pressure increases. At lower pressures the 2.1 mm location has a lower temperature than in the case of lower O/F.

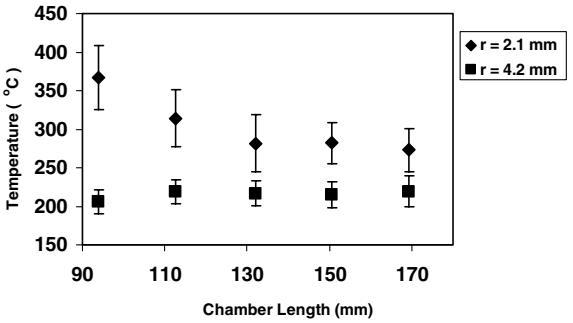

Fig. 15 Effect of chamber length on the injector face temperatures at $O/F = 4$ and $P_{\text{chamber}} = 4.9$ MPa. As the chamber length increases the temperature closer to the injector decreases. Farther away from the injector the temperature is less sensitive.

temperatures are closer than in the case of the lower mass flow recorded in Fig. 13. This suggests that considerable changes in the flow pattern of the recirculation exist both in space and, given the range of temperature fluctuation, in time. These fluctuations were identified in computational studies, such as [3], and are of particular interest because they are closely coupled to the jet mixing and, therefore, affect the overall chamber dynamics.

The chamber length effect on the injector face temperature results, as well, from the recirculation pattern. This effect is shown in Fig. 15. The temperature measured at 4.2 mm from the center axis shows little change with a decrease in chamber length. The temperature measured at 2.1 mm, however, shows a sizable increase as the chamber length decreases. This increase can be due to hotter gases in the recirculation region as the chamber length decreases or to an accelerated recirculation in the shorter chamber.

IV. Summary

A high-pressure facility with optical access has been built and instrumented to cover a range of experimental conditions for single, coaxial, gaseous jets. The results of wall heat flux measurements for a range of pressures and mass flows indicated the following:

1) Maximum heat release occurs around 60 mm, or $30d_j$ from the injector face.

2) The heat flux and chamber wall temperature distributions seem to have no direct pressure dependence and only a slight dependence on propellant injection velocities, however, a strong dependence on mass flows is noted.

3) The lack of pressure dependence and only slight dependence on the propellant injection velocities, as shown by the similarity in heat flux profiles, suggests that the basic dynamic structures of the combusting flow are mainly dominated by geometrical effects.

4) A scaling of heat flux values with the square root of fuel mass flow rate, instead of chamber pressure, is suggested for a simplified, first order scaling.

5) The injector face temperatures exhibit large time fluctuations but are not affected by changing pressure except in the case of large mass flow ratios.

6) The chamber length clearly changes the recirculation pattern with longer chambers reducing the injector face temperature.

Acknowledgements

This work has been performed with support from NASA Grant NCC3-994 with Claudia Meyer as the Program Manager. K. Tucker (NASA Marshall) and J. Hulka (Jacobs Sverdrup) have provided continuous support and advice throughout the facility development and the experimental program.

References

[1] *3rd International Workshop on Rocket Combustion Modeling*, Paris, France, 2006.

[2] Tucker, K., West, J., Williams, R., Lin, J., Rocker, M., Canabal, F., Robles, B., and Garcia, R., "Using CFD as a Rocket Injector Design Tool: Recent Progress at Marshall Space Flight Center," *5th International Symposium on Liquid Space Propulsion* [CD-ROM] 2003.

[3] Tramecourt, N., Masquelet, M., and Menon, S., "Large-Eddy Simulation of Unsteady Wall Heat Transfer in a High Pressure Combustion Chamber," AIAA Paper 2005-4124, 2005.

[4] Allen, M. G., and Miller, M. F., "Optically-Accessible Gas Turbine Combustor for High Pressure Diagnostics Validation," AIAA Paper 97-0116, 1997.

[5] Kojima, J., and Nguyen, Q-V., "Development of a High-Pressure Burner for Calibrating Optical Diagnostic Techniques," NASA TM-2003-212738, Glenn Research Center, Cleveland, OH, 2003.

[6] Carter, C. D., King, G. B., and Laurendeau, N. M., "A Combustion Facility for High-Pressure Flame Studies by Spectroscopic Methods," *Review of Scientific Instruments*, Vol. 60, No. 8, Aug. 1989, pp. 2606–2609.

[7] Locke, R. J., Hicks, Y. R., Anderson, R. C., and Ockunzzi, K. A., "OH Imaging in a Lean Burning High-Pressure Combustor," *AIAA Journal*, Vol. 34, No. 3, March 1996, pp. 622–624.

[8] Foust, M. J., Deshpande, M., Pal, S., Ni, T., Merkle, C. L., and Santoro, R. J., "Experimental and Analytical Characterization of a Shear Coaxial Combusting GO_2/GH_2 Flowfield," AIAA Paper 96-0646, 1996.

[9] Santoro, R. J., "Applications of Laser-Based Diagnostics to High Pressure Rocket and Gas Turbine Combustor Studies," AIAA Paper 1998-2698, 1998.

[10] Marshall, W. M., Pal, S., Woodward, R. D., and Santoro, R. J., "Benchmark Wall Heat Flux Data for a GO2/GH2 Single Element Combustor," AIAA Paper 2005-3572, 2005.

[11] Tucker, P. K., Klem, M. D., Smith, T. D., Farhangi, S., Fisher, S. C., and Santoro, R. J., "Design of Efficient GO2/GH2 Injectors: A NASA, Industry, and University Cooperative Effort," AIAA Paper 1997-3350, 1997.

[12] Conley, C. A., "High-Pressure GO_2/GH_2 Combustion Chamber Dynamics," M.S. Thesis, University of Florida, Gainesville, FL, 2006.

[13] Engel, V., Meijer, G., Bath, A., Andersen, P., and Schinke, R., "The $C \rightarrow A$ Emission in Water: Theory and Experiment," *Journal of Chemical Physics*, Vol. 8, Oct. 1987, pp. 4310–4313.

[14] Deshpande, M., and Merkle, C. L., "Characterization of Unsteady Effects in GO2/GH2 Combustor Flowfields," AIAA Paper 1996-3128, 1996.

T. Lin
Associate Editor